



Towards the prominent cocatalytic effect of ultra-small CoP particles anchored on g-C₃N₄ nanosheets for visible light driven photocatalytic H₂ production

Bing Luo, Rui Song, Jiafeng Geng, Xiaohe Liu, Dengwei Jing*, Menglong Wang, Cheng Cheng

International Research Center for Renewable Energy & State Key Laboratory of Multiphase Flow in Power Engineering, Xi'an Jiaotong University, Xi'an, 710049, China



ARTICLE INFO

Keywords:
Noble metal free
Quantum dots
Graphitic carbon nitride
Photocatalytic H₂ generation

ABSTRACT

In this work, we prepared a series of novel quasi 0D/2D nanohybrids of CoP/g-C₃N₄ derived from the composites of Co₃O₄ quantum dots with g-C₃N₄ nanosheets. Particularly, 0.45 wt% CoP modified g-C₃N₄ had the highest H₂ generation rate as 1.074 mmol·h⁻¹ g⁻¹ (AQY: 6.1% at 420 nm) under visible light irradiation, which was 283 and 5 times of that for pure g-C₃N₄ (0.0038 mmol·h⁻¹ g⁻¹) and 0.5 wt% Pt/g-C₃N₄ (0.216 mmol·h⁻¹ g⁻¹), respectively. The excellent performance was attributed to the formation of a new electron transfer route owing to the interaction of Co atoms with N atoms, the reaction sites of metal-like Co-P bonds due to the lower energy barrier than Pt toward H₂ evolution, and finally the well dispersed CoP nanoparticles offering much more reaction sites than bulk counterpart. Our work provides a new methodology to construct highly dispersed noble metal free cocatalyst in the matrix of host photocatalyst with excellent performance.

1. Introduction

Converting solar energy into clean hydrogen via photocatalysis is a promising method to fulfill the increasing worldwide demands of energy, as well as the environmental issues aroused by the burning of fossil fuels [1–4]. Tremendous photocatalytic materials have been developed as catalysts for H₂ production since the discovery of photo-induced water splitting on an n-type TiO₂ [5]. However, most semiconductors don't possess satisfied efficiency without the existence of cocatalyst even with sacrificial reagent, one of reason, because of the high recombination efficiency of excited electron/hole pairs before migrating to the surface for reactions. Another important reason is that the surface reaction is too sluggish to efficiently consume the hot carriers. Generally, for the purpose of dragging the electrons out to the surface, thus noble metals (such as Pt, Au) are used as the cocatalysts. Noble metals not only act as electron sinks, but also provide abundant water reduction sites, hence dramatically enhance H⁺ reduction reaction [4]. While the rarity and high cost of such noble metals limit their scalable application in practice [4], therefore, encouraging the search of valueless candidates to replace noble metals.

To date, extensive researches have reported earth abundant elements based materials to substitute noble metal catalysts for H₂ generation [6,7]. For instance, metal Ni or Co particles deposited on the surface of semiconductors [8–13] acting as electrons acceptor lead to

drastic improvement on H₂ production in the presence of sacrificial reagents. Moreover, metal chalcogenides, such as NiS_x [14,15], CoS_x [16,17], MoS₂ [18–20], are also extensively employed in solar energy driven H₂ evolution process. Among these potential candidates, transition metal phosphides have attracted significant interest due to the excellent electricity and heat conductive ability, good chemical and thermal stability, strong reduction ability, low overpotential [21]. Most importantly, base sites of P can effectively trap the positively charged protons and limit the electrons delocalization in the metal, thus significantly improve the H₂ production [21,22]. Thus, many pioneering researches have investigated the outstanding merits of utilizing metal phosphides as cocatalysts in the photocatalytic H₂ generation processes [23–26].

On the other hand, graphitic carbon nitride (g-C₃N₄) as an emerging star in photocatalysis has demonstrated a bright future in the solar energy conversion reactions due to its attractive characteristics including unique layered structure, earth abundance, chemical stability, nontoxicity, visible light harvesting capacity, and also proper electronic structure for water reduction [27–30]. However, the quick recombination of photogenerated charges and sluggish reaction kinetics inevitably result in the unsatisfied catalytic performance [27,31,32]. It has been reported that the modification of g-C₃N₄ by metal phosphides can effectively promote the HER performance [33–36]. Thereinto, for CoP, the density function theory simulation reveals that the desorption

* Corresponding author.

E-mail address: dwjing@mail.xjtu.edu.cn (D. Jing).

of H₂ from the CoP surface is easier than the noble metal Pt, indicating that CoP is a great promising cocatalyst for H₂ production [37]. It is worth noting that several CoP/g-C₃N₄ composites in different CoP preparation methods have been reported to produce H₂ [35,38,39]. However, CoP preparing methods employed in these work result in the unsatisfied catalytic ability. Thus, the synthesis and hybridization of metal phosphides with the purpose of achieving good catalytic performance still remain as a challenge in the g-C₃N₄ nanohybrids. Notably, to develop a convenient method to combine metal phosphides nanoparticles with g-C₃N₄ host for the intimate contact heterojunction for boosting photocatalytic performance has become a stumbling block and a burgeoning challenge [40] simultaneously with well-crystallized, and highly dispersed nanosized particles.

Inspired by aforementioned discussion, herein, we developed an electrostatic driven self-assembly method to incorporate zero-dimensional nanocrystalline Co₃O₄ QDs into two-dimensional g-C₃N₄ nanosheets, which was further converted to quasi 0D CoP by phosphorization method. Herein, CoP nanocrystals intimately contacted with g-C₃N₄ nanosheets exhibiting drastically promoted H₂ production under visible light irradiation without the assistance of noble metals. And 5 times higher H₂ evolution rate than that of same mass Pt modified g-C₃N₄ was achieved by this new approach. It was elucidated that the good catalytic performance came from the synergistic effect of N-Co interactions between g-C₃N₄ and CoP via accelerating the photo-induced charge carriers' separation/migration, and also the metallic characteristics of Co-P bonds by acting as H₂ evolution sites. It is expected that our work will shed bright light on the development of effectively active and photocatalyst for H₂ evolution.

2. Experimental

2.1. Materials and synthesis

The preparation of g-C₃N₄ nanosheets. g-C₃N₄ nanosheets were synthesized by thermal condensation using urea as precursor. In detail, 25 g urea powder was placed in a corundum crucible equipped with a cover, and calcined for 4 h at 600 °C in the air atmosphere with an increasing temperature rate as 5 °C/min. Grounded the obtained pale yellow powder into fine powder and labeled it as CN. Finally, 0.774 g CN was obtained, corresponding to a production yield of 3.1%.

The preparation of Co₃O₄ quantum dots (QDs). Co₃O₄ QDs were synthesized according to a recent report work [41]. Where 0.16 g Co (Ac)₂·4H₂O was put into 7 ml benzyl alcohol contained in a three-necked flask. Then the mixture was kept stirring until the complete dissolution of Co(Ac)₂·4H₂O powder at room temperature. Then, 7 ml NH₃·H₂O (25%) aqueous solution was dropwise added into the above solution with vigorous stirring. The reddish suspension contained in the vessel was placed into an oil bath set at 165 °C for reacting 2 h under continuous stirring. And a black suspension was obtained. Finally, 7 mL diethyl ether was added into the final reaction suspension. And the black precipitate was washed with ethanol several times via centrifugation, and, at last, re-dispersed into ethanol with a mass concentration designed as 4 mg/mL.

The synthesis of Co₃O₄ QDs/g-C₃N₄ samples. 0.1 g g-C₃N₄ was dispersed into 10 mL ethanol. The suspension was sonicated for 30 min to prepare a well dispersed mixture. Then, certain amount Co₃O₄ QDs solution was injected into above suspension, which was sonicated for another 30 min and successively stirred for 2 h. Next, the mixture was centrifuged at 3000 rpm to collect the Co₃O₄ QDs/g-C₃N₄ composites, which was labelled as Co₃O₄/CN. A series of samples were prepared with the nominal mass percentage of Co₃O₄ to be 0.2, 0.4, 0.8, and 1.6 wt%, respectively.

The synthesis of CoO/g-C₃N₄ and CoP/g-C₃N₄ samples. CoO/g-C₃N₄ was prepared by annealing 50 mg Co₃O₄ QDs/g-C₃N₄ composite via a muffle in the air at 300 °C for 2 h with an increasing temperature rate as 5 °C/min, and labeled as CoO/CN, in which CoO was confirmed by the

high resolution TEM characterization. Regarding the synthesis of CoP/g-C₃N₄, 50 mg Co₃O₄ QDs/g-C₃N₄ composite was evenly placed at the downstream of a porcelain boat. And 250 mg NaH₂PO₂·H₂O as the source of phosphorus was put at the upstream of the porcelain boat. Then, they were annealed under the same conditions for CoO/CN preparation except for the presence of Ar atmosphere. Here, the theoretical mass loading of CoO is 0.19, 0.37, 0.75, and 1.49 wt%, respectively, assuming Co₃O₄ was totally converted into CoO. The final product was labeled as CoP/CN, which has a nominal mass loading of CoP of 0.23, 0.45, 0.90, and 1.80 wt%, respectively, after total conversion of Co₃O₄ into CoP.

2.2. Material characterizations

Zeta potential tests were carried out on Zetasizer Nano-ZS90 apparatus, Malvern Instrument. Ethanol was employed the base liquid containing g-C₃N₄ or Co₃O₄ QDs. The crystalline structure information of all catalysts were collected by an X-ray diffraction (XRD) diffractometer (PANalytical X'pert MPD Pro, Netherlands). Transmission electron microscopy (TEM) images were recorded via a 300 kV accelerating voltage (FEI Tecnai G2F30 S-Twin, USA). Fourier transform infrared (FT-IR) spectra were tested by an FTIR spectrophotometer (Bruker Vetex70, Germany). Specific surface area and pores structure information were performed using porosimetry analyzer through N₂ adsorption-desorption analysis (Micromeritics ASAP 2020, USA). X-ray photoelectron spectroscopy (XPS) were tested using an X-ray photoelectron spectroscope via a monochromatic Al K α line source ($\text{h}\nu = 1486.69 \text{ eV}$) (Kratos Axis Ultra DLD, Japan), where the standard C 1s peak centered at 284.8 eV was utilized as the reference. UV-vis absorbance spectra of prepared samples were measured using a UV-vis-NIR spectrophotometer (Cary 5000, Agilent). Photoluminescence spectra (PL) were performed with 317 nm excitation light at room temperature by PTI QuantaMaster 40 (USA) steady-state fluorescence spectrophotometer.

2.3. Photoelectrochemical tests

Photophysicschemical properties of all samples were examined by the photoelectrochemical measurements conducted on a three-electrode cell equipped with reference electrode (Ag/AgCl), counter electrode (Pt plate), and an FTO glass plate loading photocatalyst as working electrode. Neutral Na₂SO₄ (0.5 M, pH = 6.8) aqueous solution was selected as the electrolyte for conducting charges. Specially, bias voltage was set as 0.4 V vs Ag/AgCl in the transient photocurrent densities measurements. Electrolyte and bias voltage were kept the same during the electrochemical impedance spectra (EIS) tests with AM 1.5 illumination, the frequency ranges from 100 kHz to 0.1 Hz. Mott-Schottky (MS) measurements were carried out in the dark condition with 1 KHz frequency. The potential vs RHE converted from the potential vs Ag/AgCl by using the equation below.

$$E_{\text{RHE}} = E_{\text{Ag/AgCl}} + 0.059 \times \text{pH} + E^{\circ}_{\text{Ag/AgCl}} \quad (1)$$

Where E_{Ag/AgCl} is the applied voltage, and E[°]_{Ag/AgCl} is 0.1976 V at 25 °C.

Moreover, the working electrode was fabricated as following procedure: a suspension consisting of 1 mg catalyst, 250 μL ethanol, 250 μL deionized water, and 10 μL DuPont D1020 Nafion solutions (10 wt%) was dispersed by ultrasonic for 30 min. Then 100 μL of the above prepared suspension mixture was dripped uniformly on a cleaned FTO glass with a size of 1.5 × 1.5 cm². The work electrode was dried naturally in the air at room temperature.

2.4. Photocatalytic H₂ production measurements

Visible light driven photocatalytic H₂ evolution was conducted on a side-irradiation Pyrex photoreactor. The simulated light source used a

300 W Xenon lamp and a UV cut-off filter to remove the light with wavelength smaller than 420 nm. A syringe was used to sample the produced gas every 30 min for the quantitatively analysis via a gas chromatograph (Ar as a carrier gas, NaX zeolite column) equipped with thermal conductivity detector (TCD). In the photocatalytic H₂ production test, 10 mg catalyst was placed into 80 mL aqueous solution including sacrificial reagent (triethanolamine (TEOA), 10% v/v). Before starting the photocatalytic test, the suspension was purged with N₂ to completely remove the dissolved oxygen in the solution. And the reaction was conducted at room temperature. Furthermore, in the stability tests, after finishing a cycle, the produced H₂ was removed by purging N₂ for 20 min, and then the next cycle was continued without adding additional fresh TEOA into the reactor due to the existence of excess amount of TEOA.

The apparent quantum yield (AQY) test was carried out under illumination of the 300 W Xe lamp with a band-pass filter (420 ± 5 nm). The power of incident light was measured by a spectroradiometer (Avantes AvaSpec-2048-USB2, Netherlands). The equation for AQY calculation is shown as following [29]:

$$\text{AQY} (\%) = \frac{\text{number of reacted electrons}}{\text{number of incident photons}} \times 100 \\ = \frac{2 \times \text{number of evolved H}_2 \text{ molecules}}{\text{number of incident photons}} \times 100 \quad (2)$$

The turnover number (TON) can be calculated based on the following equation [26]:

$$\text{TON} = \frac{\text{Moles of evolved H}_2}{\text{Moles of CoP on photocatalyst}} \quad (3)$$

3. Results and discussion

In order to prepare well dispersed hybrids, Co₃O₄ QDs and g-C₃N₄ nanosheets were prepared firstly, respectively, and then hybridized via electrostatic self-assembly method with the assistance of ultrasonic and stirring. As shown in the Fig. 1, g-C₃N₄ and Co₃O₄ QD in the ethanol owns a negative and positive charged surface, with a corresponding Zeta potential of -8.67 mV and 24.9 mV, respectively. Therefore, they should have great tendency to spontaneously assemble into composites by at least the Coulomb attraction due to the opposite charged surface, besides of some other possible molecular forces such as the Van der Waals forces. Regarding CoP/CN, it was fabricated by converting Co₃O₄ to CoP through phosphorization using NaH₂PO₂·H₂O as phosphorus source by pyrolysis. The flowchart is displayed in the Fig. S1. Thereinto, g-C₃N₄ prepared by urea via thermal condensation exhibits

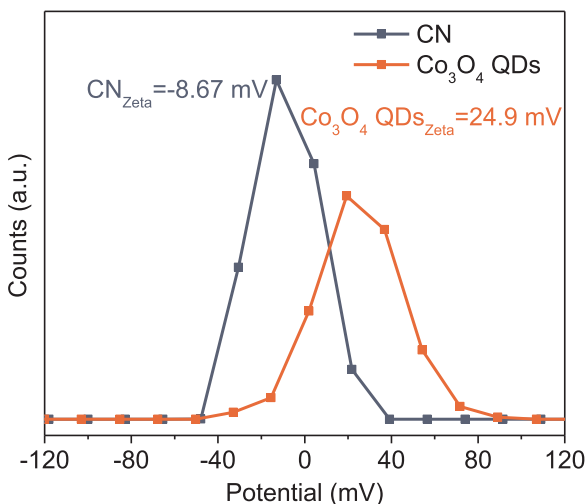


Fig. 1. The Zeta potential of CN and Co₃O₄ QDs in ethanol.

characteristic crumpled layered structure (Fig. 2a). And Co₃O₄ QDs were synthesized through a one-step oil-bath-assisted heat treatment of the mixture of Co(Ac)₂·4H₂O, benzyl alcohol, and ammonium hydroxide [41]. The size distribution of Co₃O₄ QDs falls in the range of 5–10 nm without aggregation (Fig. 2b), indicating the well dispersion of Co₃O₄ QDs in ethanol. The spacing of lattice 0.202 nm and 0.237 nm is assigned to the (100) and (311) crystal plane of Co₃O₄, respectively (Fig. 2c) [37,42]. X-ray diffraction patterns (Fig. S2) further confirm the successfully synthesized cubic Co₃O₄ (JCPDS 00-043-1003), which shows a strong signal at 2θ at 36.8°, responding to (311) crystal plane [37]. After being coupled with g-C₃N₄ via electrostatic self-assembly in the ethanol solution, these Co₃O₄ QDs tended to form aggregates. This consequence may be caused by the high surface energy of QDs due to the existence of a large part of chemically unsaturated atoms on their surfaces [41]. Because in the preparation process of Co₃O₄/CN, the further removing of benzyl alcohol molecule from the surface of Co₃O₄ QDs lead to the instability, and thus the slight aggregation. Obviously, these slightly agglomerated Co₃O₄ QDs are also anchored on g-C₃N₄ substrate uniformly. Fortunately, the Co₃O₄ QDs on g-C₃N₄ still have sizes smaller than 20 nm, even after aggregation (Fig. S3a). And as shown by our following photocatalytic activity tests, this hybrid material still showed very good activity indicating the calcination condition should be near the optimal one. The thermal treatments of hybrids Co₃O₄/CN in the air or in the phosphorization process under Ar protection did not change the morphology of Co-species/CN, as shown in the Fig. S3b, c and Fig. 2d, and f. Co₃O₄ particles were converted to CoO in the air, proved by the HRTEM image (Fig. 2e), where simultaneously contains the lattice space of 0.243 nm and 0.212 nm, indexed by the crystal plane (111) and (200) of CoO, respectively [43–45]. Regarding Co₃O₄ particles in phosphorization process, they reacted with PH₃, which was released by the pyrolysis of NaH₂PO₂·H₂O, and were converted completely to CoP particles revealed by the coexistence of lattice planes (111) and (211) of CoP, responding to interplanar distance as 0.248 nm and 0.187 nm in the Fig. 2g, respectively [37,46,47]. Moreover, the well dispersed nanoparticles anchoring on g-C₃N₄ hosts can be further proved by the HADDF images, as well as the elemental mapping results (Fig. 2h, i) of CoO/CN and CoP/CN. Meanwhile, signals owing to element P exist locally at the spots of Co element, consequently, directly reflecting the transformation of Co₃O₄ to cobalt phosphides. It is worth noting that, in the hybridization composite, with same mass loading of CoP, these ultra-small nanoparticles can offer more reaction sites, and also contact with supporters much more intimate than the bulk CoP particles, which would in turn to facilitate reaction in the photocatalysis.

The X-ray diffraction patterns of CN, CoO/CN, and CoP/CN are displayed in the Fig. 3a. XRD pattern for each sample contains two typical diffraction peaks of g-C₃N₄, which centering at 12.8° (100) and 27.6° (002) is attributed to the intralayer packing motif of heptazine units and the interlayer periodic stacking along the c-axis controlled by the van der Waals forces, respectively [48,49]. No detectable diffraction signals owing to CoO or CoP are recorded due to their weak dosage (lower than 0.5 wt% in the composites). Moreover, the Fourier transform infrared (FTIR) results of CN, CoO/CN, and CoP/CN in Fig. 3b exhibit signal at 810 cm⁻¹ assigned to the breathing modes of the tri-triazine units, fingerprints of NH/NH₂ stretching modes between 2900 and 3340 cm⁻¹, and peaks ranging from 3400 to 3600 cm⁻¹ because of the broad band of hydroxyl group/adsorbed water, respectively. Additionally, strong absorption for stretching modes of CN heterocycles exist in the range of 1200–1600 cm⁻¹ range [30,50]. Consequently, both of XRD and FTIR consequences indicate that g-C₃N₄ retains primary structure after sustaining the calcination process in the air or phosphorization process. While the information of CoO and CoP can not be detected due to their low dosages. The pore structures and Brunauer-Emmett-Teller (BET) surface areas of all catalysts were analyzed by N₂ adsorption-desorption measurements at 77 K. All samples exhibit a high adsorption capacity in the high relative pressure (P/P₀ > 0.6)

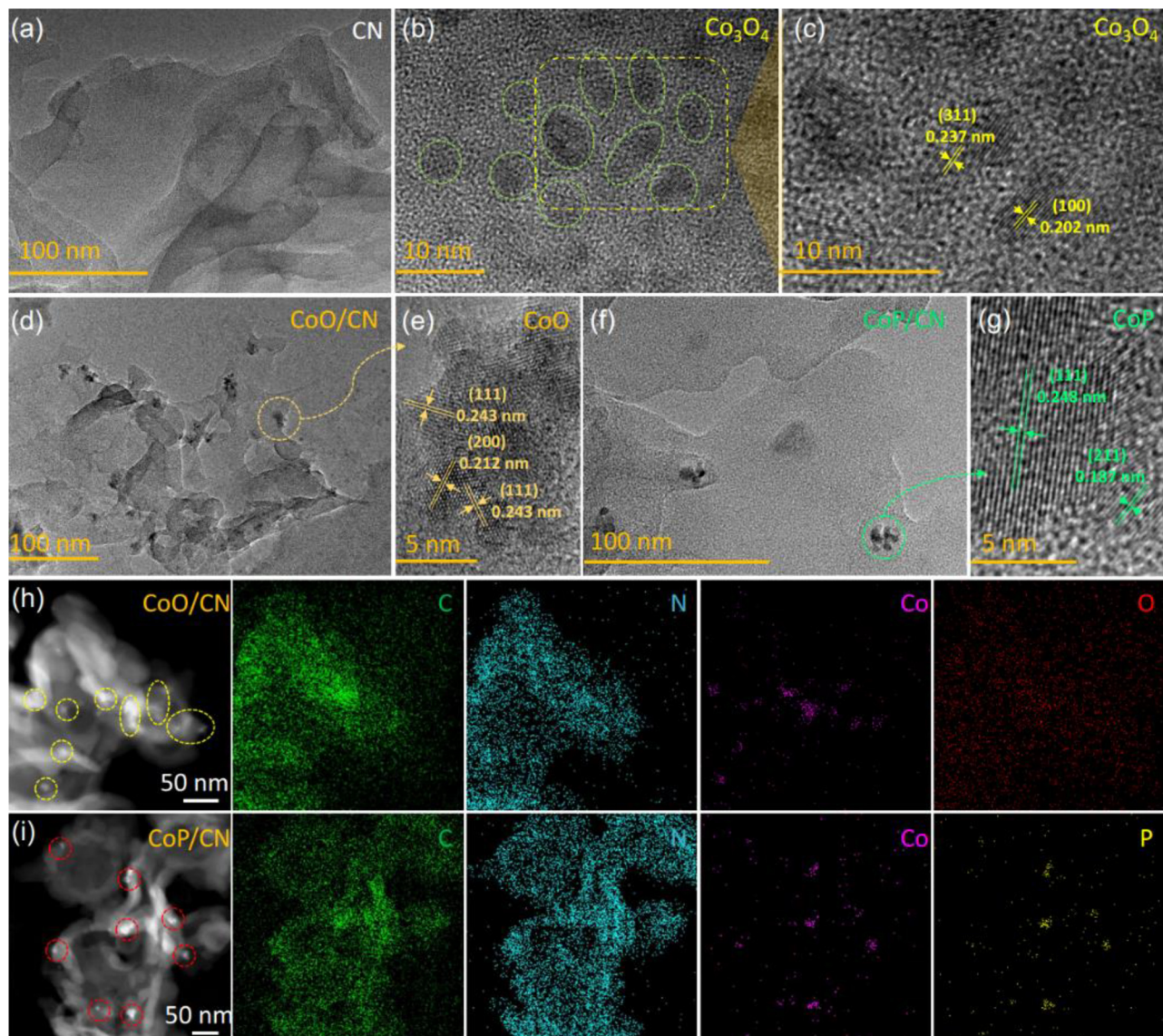


Fig. 2. The TEM images of (a) $\text{g-C}_3\text{N}_4$, (b) Co_3O_4 quantum dots, (d) CoO/CN composites and (f) CoP/CN composites. The HRTEM images of (c) Co_3O_4 , (e) CoO , and (g) CoP particles. The STEM images and elemental mapping results of (h) CoO/CN with element C, N, Co and O; and (i) CoP/CN with element C, N, Co, and P.

attributed to a typical IV isotherm, implying the presence of plentiful mesopores [51], further proved by the pore size distribution results (the size of almost pores falls in 2–5 nm) in the inset of Fig. 3c. Moreover, compared with pure CN, CoO/CN and CoP/CN owning the almost same surface area implies that the loading of CoO and CoP nanoparticles does

not block the pores of $\text{g-C}_3\text{N}_4$. Generally, the existence of pores for catalysts always contributes to the photocatalytic H_2 evolution reaction due to the shortened length of charge carrier immigration path, as well as their facilitating effect on mass transfer of reactant molecular in the reaction solution [48].

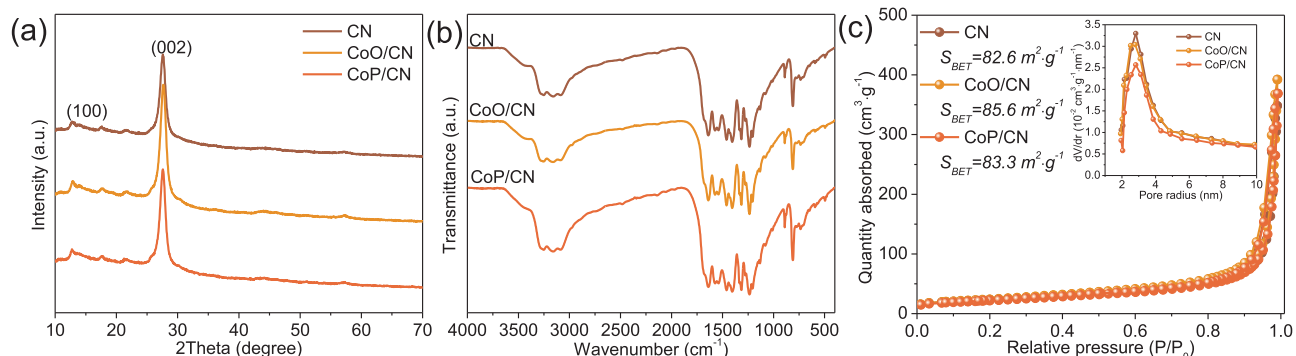


Fig. 3. The (a) XRD patterns, (b) FTIR spectra, and (c) N_2 adsorption and desorption curves, BET surface areas, and pores distributions of CN, CoO/CN , and CoP/CN .

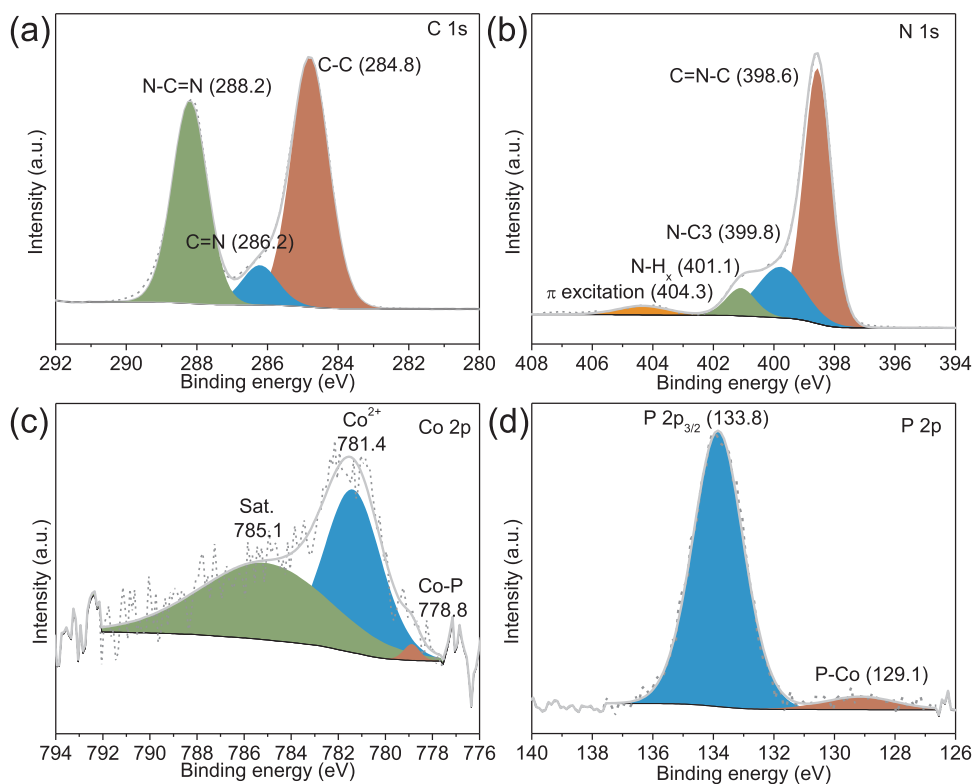


Fig. 4. The XPS spectra of (a) C 1s, (b) N 1s, (c) Co 2p_{3/2}, and (d) P 2p for CoP/CN (1.8 wt% CoP).

For elucidating the surface chemical compositions of CoP/CN and the interactions between two components, CN and CoP/CN were investigated by X-ray photoelectron spectroscopy. It is worth noting that, 1.8 wt% CoP/CN was selected as model catalyst, because the lower loading of CoP would result in the undetectable signals for element Co and P. The high resolution C 1s spectrum (Fig. 4a) of CoP/CN have three signals at 284.8, 286.2, and 288.2 eV, representing adventitious C, C-N-H_x, and N-C≡N coordination [16,28,52], respectively. Regarding the high resolution N 1s spectra (Fig. 4b), there are four signals at 398.6, 399.8, 401.1, and 404.3 eV corresponding to sp²-bonded nitrogen (C≡N=C), tertiary nitrogen (N-C3), amino groups (N-H_x), and π excitations [50,53], respectively. Both of C 1s and N 1s spectra prove the retained primary structure of g-C₃N₄ after loading CoP. As reported, single Co atom tends to form Co-N₄ site with the N atoms in the C = N-C [54]. In our case, compared with the CN (Fig. S4 and Table. S1), the decreased C = N-C intensity confirms the intensive interaction of Co with N. On the other hand, the absence of signal at 560 cm⁻¹ in the FTIR spectra excludes the possible C-P interaction in the CoP/CN [55,56]. Moreover, the weak signal at 778.8 eV in the high-resolution spectrum of Co 2p (Fig. 4c) should be the index of Co-P bonds in CoP, which is similar to that of the metallic Co (2p_{3/2}, 777.9 eV) [37]. Furthermore, oxidized species resulting from superficial oxidation of CoP is detected at 781.4 eV belonging to the Co 2p_{3/2} of Co²⁺, as well as a satellite at 785.1 eV [53]. For better comparison, the Co 2p of CoO/CN is shown in the Fig. S5. Obviously, the peak of Co 2p_{3/2} has a large positive shift from 779.6 eV of CoO to 781.5 eV of CoP, indicating the dramatic change of coordination environment of Co atoms. From the high resolution of Co 2p of CoO/CN, no metallic-like component of Co can be detected. Clearly, CoO/CN lacks the metallic-like Co, which could be the active reaction sites in a photocatalytic reaction [37]. For P 2p, the peak at 129.1 eV belongs to P-Co in CoP (Fig. 4d) [37]. While the peak at 133.8 eV is the oxidized P due to the inevitable surface oxidation, which has been reported in other papers [26,57]. Furthermore, XPS spectrum for CN subjected to a similar phosphorization process without loading of Co₃O₄, labeled as sample P-CN, has been

recorded to examine the possible P. As shown in the Fig. S6, only a weak P signal was recorded and even this weak signal should be from the adsorbed P. Thus, it can be safely inferred that P element is hard to be introduced into CN structure during the phosphorization process because of the method properly chosen to fabricate CoP/CN. Accordingly, above analysis confirms that neither Co nor P were doped into g-C₃N₄ when CoP was introduced via a phosphorization process of Co₃O₄. Meanwhile it also proves the existence of metal-like characteristics Co-P bonds in the CoP/CN, which contributes to H₂ evolution [21,37,58].

Additionally, the spectra of O 1s for CN, CoO/CN, and CoP/CN are displayed in the Fig. 5. Thereinto, O 1s for the CN has a core level at 531.9 eV (Fig. 5a) assigned to the adsorbed H₂O. While the O 1s peak at 533.2 refers to the O=C bonds [59]. In the Fig. 5b and c, the O 1s spectra of CoO/CN and CoP/CN have a slight positive shift, indicating the interaction between g-C₃N₄ and CoO and CoP. Moreover, another peak centred at 529.8 eV owing to Co-O bonds of CoO was detected for the sample CoO/CN [60]. No Co-O bonds detected in the CoP/CN rule out the formation of CoO_x in the CoP/CN.

To measure the photocatalytic performance of CoP/CN, the optimal mass loading of CoP was first studied under visible light illumination with TEOA as sacrificial reagent. In the Fig. 6a and b, within the 3 h measurement, pure CN shows poor catalytic ability with hydrogen evolution rate (HER) as 3.8 μmol h⁻¹ g⁻¹. After anchoring different mass percentage of CoP, each CoP/CN shows significantly improved HER. Thereinto, 0.45 wt% CoP/CN has the highest HER as 1.074 mmol·h⁻¹ g⁻¹. It is 283 times of pure CN. Meanwhile, it also has an outstanding AQY of 6.1% at 420 nm over the optimal g-C₃N₄ based photocatalytic systems without noble metals. Moreover, 0.5 wt% Pt/CN and 1 wt% Pt/CN prepared by in situ photo-deposition method, and CoO/CN shows a HER as 0.216, 0.379, and 0 mmol·h⁻¹ g⁻¹, respectively. These consequences imply that HER of 0.45 wt% CoP/CN is almost 5 times of g-C₃N₄ loading with almost same mass weight Pt (0.5 wt % Pt/CN), as well as 2.8 times of 1 wt% Pt/CN. The better H₂ evolution performance of CoP/CN than Pt/CN has been revealed by the density function theory (DFT) simulation [37]. Because the removal of H₂ from

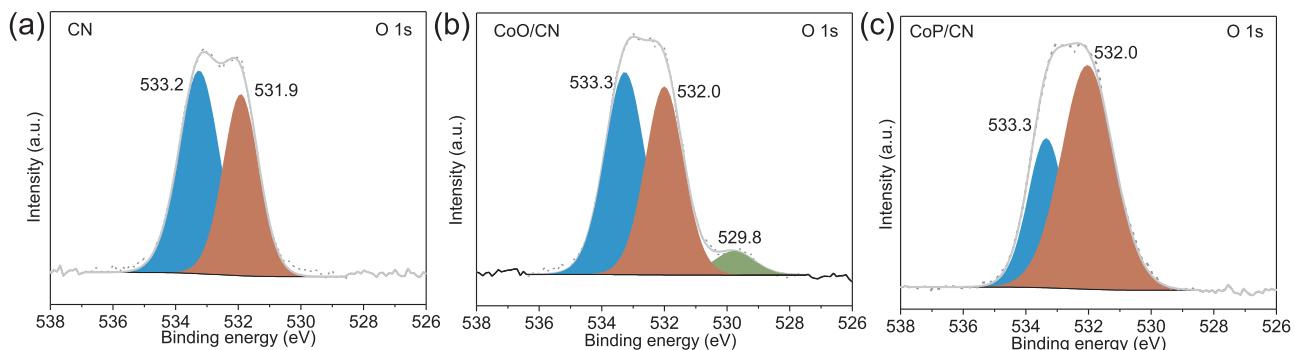


Fig. 5. The XPS spectra of O 1s of (a) CN, (b) CoO/CN (1.49 wt% CoO), (c) and CoP/CN (1.8 wt% CoP), respectively.

the CoP surface needs to overcome an energy of 0.63 eV, which is lower than that of noble metal Pt (0.74–0.86 eV) [37,61,62]. However, bulk cobalt phosphides with large particle size only show almost the same catalytic ability with the identical mass loading Pt/CN as reported [35,39]. While in our work, the 5 times higher catalytic performance than noble metal Pt strengthened the advantages of well dispersed ultra-small CoP in the hybrids, which proved the importance of method to be employed to introduce cocatalysts into the photocatalytic system. The comparison of our work with other reported researches, employing other fabrication methods, of photacatalytic H₂ evolution performance of CoP_x/CN composites is concluded in the Fig. S7 and Table. S2.

Additionally, for better comparison, a control experiment containing identical mass loading of bulk CoP particles in the hybrids for photocatalytic H₂ production was carried out. The bulk CoP was derived from Co(OH)₂ powder, which was prepared according to a reported work [63]. The synthesized Co(OH)₂ was anchored on the surface of CN by being dispersed in the ethanol suspension and then was transformed to CoP in a same phosphorization procedure. As can be seen in the Fig. S8, no CoP XRD signals can be detected in the composite due to the low contents. Thus, a pure CoP prepared by Co(OH)₂ powder was fabricated to confirm the formation of CoP in the hybrids.

Obviously, no other impurities were tested in the Co(OH)₂ derived CoP. Corresponding photocatalytic HER results displayed in the Fig. S9, the identical mass loading of bulk CoP only leads to 7 times improvement over HER, compared to that of CN. Meanwhile, compared to 0.5 wt% Pt/CN, 0.5 wt% Pt/P-CN and 0.5 wt% Pt/Ar-CN demonstrate improved HER. The almost similar HER of 0.5 wt% Pt/P-CN and 0.5 wt% Pt/Ar-CN indicate that the main contribution of promoted photocatalytic ability can be attributed to the thermal treatment. It further rules out the possibility of P doping into g-C₃N₄ structure via the used phosphorization method in our work.

Furthermore, the turn over number (TON) of CoP/CN and Pt/CN was calculated to get more information to understand the reaction process (Fig. 6c). The TON of 0.5 wt% Pt/CN, 1 wt% Pt/CN, and 0.45 wt % CoP/CN is 25.3, 22.2, and 64.4 in 3 h reaction, respectively, as well as indicating the much better catalytic ability of CoP, especially strengthened the importance of the CoP preparation method. In addition, the photocatalytic H₂ production tests of CN, 0.5 wt% Pt/CN, and 0.45 wt% CoP/CN, respectively, were also conducted under full spectra irradiation of solar simulator. Corresponding results were recorded and shown in the Fig. S10, where 287.2, 111.7, and 1.02 μmol H₂ was obtained for 0.45 wt% CoP/CN, 0.5 wt% Pt/CN, and pure CN,

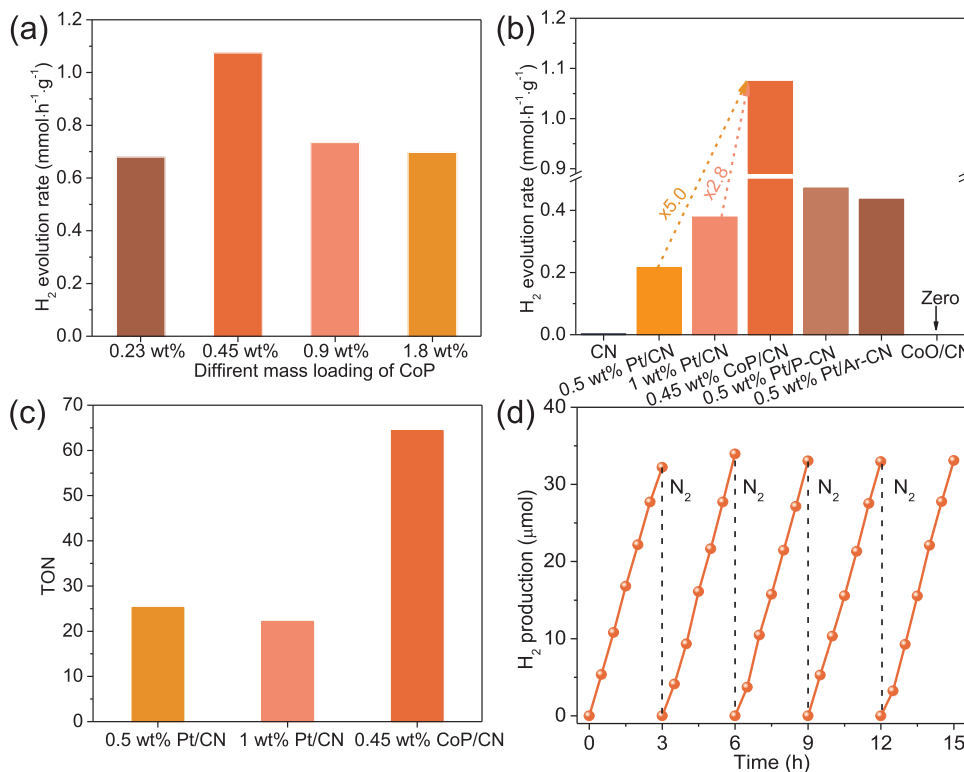


Fig. 6. (a) The average H₂ evolution rate (HER) of different mass loading of CoP on g-C₃N₄ during the 3 h reaction. (b) The comparison of HER of pure CN, 0.5 wt% Pt/CN, 1 wt% Pt/CN, 0.45 wt% CoP/CN, 0.5 wt% Pt/P-CN, 0.5 wt% Pt/Ar-CN, and CoO/CN. (c) The TON of 0.5 wt% Pt/CN, 1 wt% Pt/CN, and 0.45 wt% CoP/CN within 3 h reaction. (d) The photocatalytic stability tests of 0.45 wt% CoP/CN.

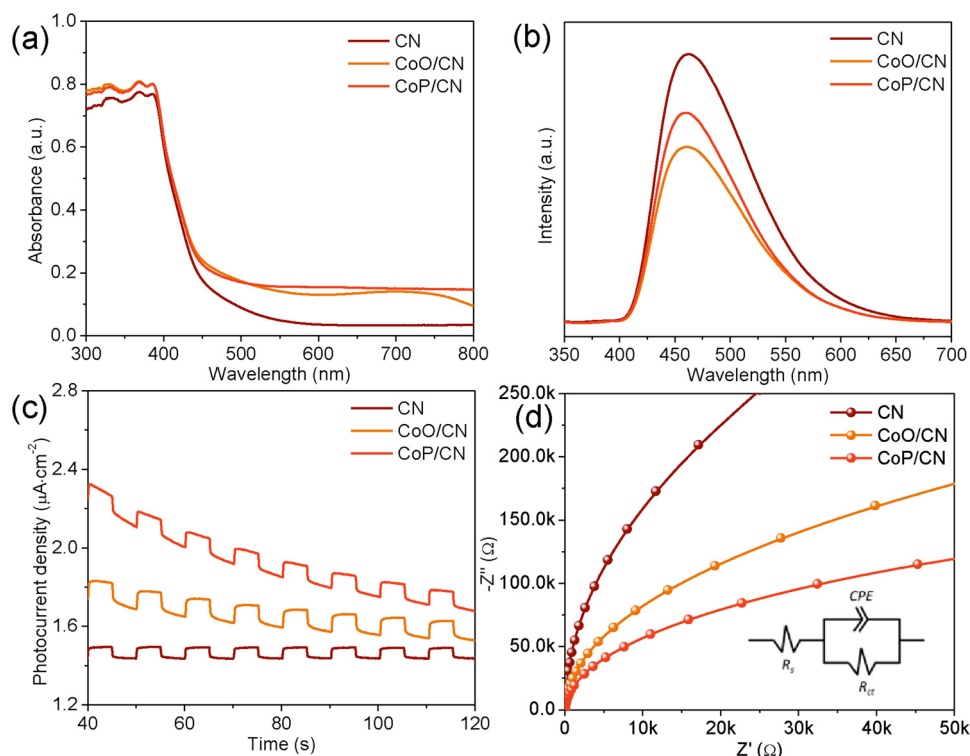


Fig. 7. (a) The UV–vis absorbance spectra, (b) steady state photoluminescence (PL) spectra (excited with a wavelength of 317 nm), (c) transient photocurrent density, and (d) electrochemical impedance spectra (EIS) of CN, CoO/CN, and CoP/CN.

Table 1

Resistance values of R_s and R_{ct} of different samples as obtained from the EIS measurements.

Photocatalysts	R_s/Ohm	$R_{ct}/10^5 \text{ Ohm}$
CN	76.00	25.8
CoO/CN	76.11	6.95
CoP/CN	81.11	3.38

respectively. Clearly, under full spectra light irradiation, the performance of sample 0.45 wt% CoP/CN is still much better than that of 0.5 wt% Pt/CN, about 2.57 times higher. Finally, in order to prove the potential practical application of CoP/CN, its stability was examined by 5 successive runs (Fig. 6d). Where no decrease in HER was observed, implying the close contact and good chemical stability of CoP/CN. The good stability can also be proved by the TEM and HRTEM images of CoP/CN collected after several rounds of photocatalytic reaction. As shown in the Fig. S11a, CoP nanoparticles still keep intimate contact with CN nanosheets. Lattice distance of 0.248 nm indexed by (111)

proves the intact structure of CoP after several runs of photocatalytic H_2 reaction, as indicated by the Fig. S11b. This further supports the good stability of CoP/CN.

In the following part, the generation of charge carriers and also their separation/transfer process was studied to unveil the reaction mechanism. In the Fig. 7a, all the samples show an absorption edge around 460 nm because of the $\pi-\pi^*$ transitions of conjugated heptazine units after absorbing photons [64]. CoO/CN and CoP/CN also show a slight absorption improvement over 460 nm, which is from the optical absorption contribution of CoO and CoP, respectively. Regarding the PL spectra (Fig. 7b), all samples show an emission bands around 460 nm due to the quenching of excited electrons from the bottom of the conduction band to the sub-band (or surface state) and the radiative transition from the sub-band to the top of the valence band of g-C₃N₄ [65]. It can be seen that, dramatically quenched PL intensity are observed for CoO/CN and CoP/CN, indicating that the charge recombination of is effectively suppressed after loading CoO or CoP. The higher transient photocurrents of CoO/CN and CoP/CN also prove the improved separation of photo-generated hole/electron pairs (Fig. 7c).

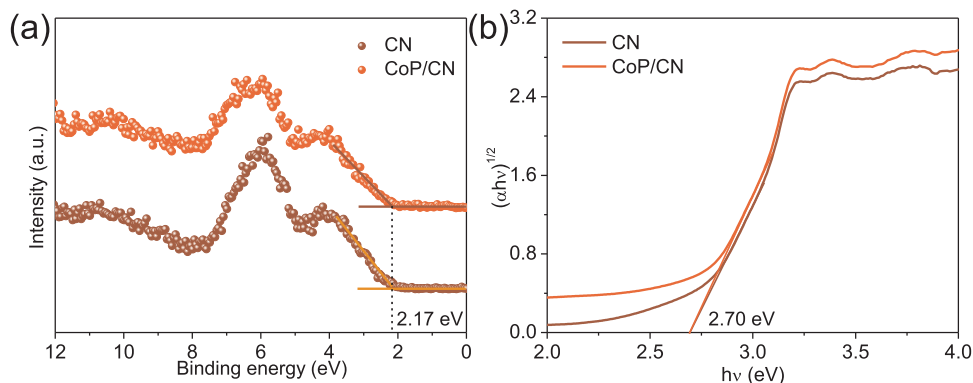


Fig. 8. (a) The valence band spectra (VBS) and (b) the K–M function of CN and CoP/CN.

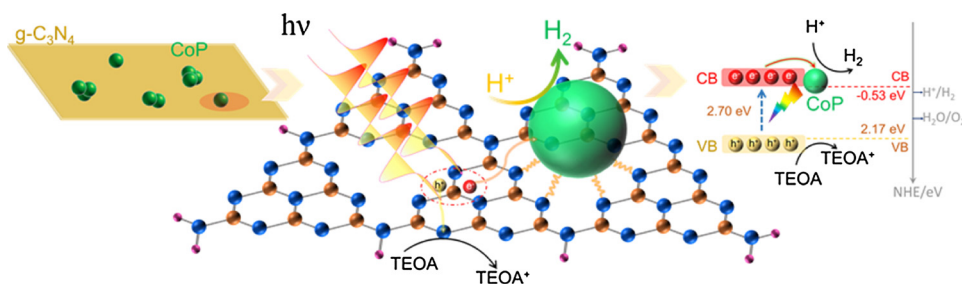


Fig. 9. The proposed schematic diagram for the photocatalytic H_2 evolution of CoP/CN.

To deeply investigate the charge transportation properties, the EIS tests were carried out and shown in the Fig. 7d. Thereinto, R_s represents the series resistance, CPE stands for the constant-phase element of electrode-electrolyte interface, and R_{ct} means the resistance for charge across the interface of electrolyte and electrode, respectively. The fitted R_s and R_{ct} are summarized in the Table 1. The R_s of all samples are almost identical due to the same preparing procedures, the same host material, as well as the same testing system. However, a few loading of CoO or CoP significantly decreased the R_{ct} , meaning the obviously decreased charge-transfer resistance across the interface of electrode and electrolyte, as well as indicating the easier charge exchange between catalysts and reaction molecule. The enhanced charge separation efficiency is beneficial for promoting the catalytic performance. Additionally, the Mott-Schottky measurements of CN, CoO/CN, and CoP/CN are given in the Fig. S12. As can be seen, CoP/CN and CoO/CN have a lower slope compared to pure CN, indicating their higher carrier concentration and the faster carrier transfer properties, which could contribute to the enhanced activity for photocatalytic H_2 production [66]. It is worth noting that the lacking of H_2 evolution cocatalysts (proved by the XPS results) in the CoO/CN results in no production of H_2 in our case, though the charge separation/transportation properties are better, and carrier concentration is higher than CoP/CN.

The VBS of CN and CoP/CN were conducted to determine the valence band maximum (VBM). As shown in the Fig. 8a, both of CN and CoP/CN have the identical VBM values of 2.17 eV. Meanwhile, according to the K-M function in the Fig. 8b, CN and CoP/CN also have the same band gaps values of 2.70 eV. Based upon the obtained VBM values and band gaps, it can be concluded that the preparation process of CoP has negligible effect on the band structure of g-C₃N₄. Accordingly, based upon the obtained VBM values and band gaps, the band structure of CoP/CN can be derived as shown in the Fig. 9.

Based on the structure analysis and charge transfer characterizations, the proposed photocatalytic H_2 generation mechanism of CoP/CN is illustrated in the Fig. 9. For the pure g-C₃N₄, it had been theoretically demonstrated that photoexcitation on g-C₃N₄ generated the e^-/h^+ pairs at the N atom sites, and the photo-induced holes remained at the N atoms for water oxidation, whereas the photoelectrons transferred to C atoms and partially remained at N atoms for H^+ reduction [67], because the lowest unoccupied molecular orbital (LUMO) is distributed on C and N atoms and the highest occupied molecular orbital (HOMO) only covers N atoms for pristine g-C₃N₄ [68–70]. However, it has poor activity due to the low charge separation efficiency, as well as the sluggish reaction kinetics [71]. After loading CoP nanoparticles, the electron transfer route is changed due to formation of Co-N bond states (proved by the XPS results) resulting from the interaction of Co atoms and N atoms [54,72], which can offer the newly constructed charge carriers separation and transportation routes for activated electrons. In detail, the photo excited electrons will transfer from N atoms to Co atoms and then participate in the proton reduction reaction on the sites of metallic Co-P bonds due to the metal-like characteristics. The energy barrier of removal of H_2 from CoP is lower than noble metal Pt [37], thus the performance is better than Pt. Furthermore, compared with the bulk CoP particles, thus 5 times higher HER performance than Pt was

obtained in our case, which is far better than other reported CoP/CN photocatalysts. On the other hand, the excited holes are consumed by oxidizing the sacrificial reagent molecule (TEOA).

4. Conclusion

In conclusion, in our work, a series CoP/CN photocatalysts have been fabricated by the phosphorization of Co₃O₄ QDs anchored on the surface of g-C₃N₄. CoP/CN with 0.45 wt% CoP has the highest HER as 1.074 mmol·h⁻¹ g⁻¹ under visible light irradiation, which is 283 and 5 times higher than that of pure g-C₃N₄ and 0.5 wt% Pt/CN, respectively. The outstanding performance was supposed to result from the formation of new electron transfer route by the interaction of Co atoms with N atoms, facilitating the charge separation and transportation of excited electrons. Moreover, the metal-like characteristics of Co-P bonds possess lower energy barrier than Pt for HER reaction, thus CoP can act as efficient H_2 formation sites. Finally, the well dispersed CoP nanoparticles offer much more reaction sites than the counterpart of bulk CoP with the same mass loading. Our work offer a new methodology to construct highly dispersed noble metal free cocatalyst with host photocatalyst by forming an excellent catalytic performance hybrid materials.

Acknowledgement

The authors gratefully acknowledge the financial supports of the National Natural Science Foundation of China (No. 51776165 and 51888103) and Newton Advanced Fellowship of the Royal Society (NA191163). This work was also supported by the China Fundamental Research Funds for the Central Universities.

Appendix A. Supplementary data

Supplementary material related to this article can be found, in the online version, at doi:<https://doi.org/10.1016/j.apcatb.2019.117819>.

References

- [1] J. Qi, W. Zhang, R. Cao, Solar-to-hydrogen energy conversion based on water splitting, *Adv. Energy Mater.* 8 (5) (2018) 1701620.
- [2] X. Wang, F. Wang, Y. Sang, H. Liu, Full-spectrum solar-light-activated photocatalysts for light-chemical energy conversion, *Adv. Energy Mater.* 7 (23) (2017) 1700473.
- [3] D. Kong, Y. Zheng, M. Kobilusz, Y. Wang, Z. Bai, W. Macyk, et al., Recent advances in visible light-driven water oxidation and reduction in suspension systems, *Mater. Today* 21 (8) (2018) 897–924.
- [4] T. Su, Q. Shao, Z. Qin, Z. Guo, Z. Wu, Role of interfaces in two-dimensional photocatalyst for water splitting, *ACS Catal.* 8 (3) (2018) 2253–2276.
- [5] A. Fujishima, K. Honda, Electrochemical photolysis of water at a semiconductor electrode, *Nature* 238 (5358) (1972) 37.
- [6] J. Ran, J. Zhang, J. Yu, M. Jaroniec, S.Z. Qiao, Earth-abundant cocatalysts for semiconductor-based photocatalytic water splitting, *Chem. Soc. Rev.* 43 (22) (2014) 7787–7812.
- [7] X. Zou, Y. Zhang, Noble metal-free hydrogen evolution catalysts for water splitting, *Chem. Soc. Rev.* 44 (15) (2015) 5148–5180.
- [8] Z. Chai, T.-T. Zeng, Q. Li, L.-Q. Lu, W.-J. Xiao, D. Xu, Efficient visible light-driven splitting of alcohols into hydrogen and corresponding carbonyl compounds over a Ni-modified CdS photocatalyst, *J. Am. Chem. Soc.* 138 (32) (2016) 10128–10131.

- [9] T. Simon, N. Bouchonville, M.J. Berr, A. Vaneski, A. Adrović, D. Volbers, et al., Redox shuttle mechanism enhances photocatalytic H₂ generation on Ni-decorated CdS nanorods, *Nat. Mater.* 13 (11) (2014) 1013.
- [10] L. Kong, Y. Dong, P. Jiang, G. Wang, H. Zhang, N. Zhao, Light-assisted rapid preparation of a Ni/g-C₃N₄ magnetic composite for robust photocatalytic H₂ evolution from water, *J. Mater. Chem. A* 4 (25) (2016) 9998–10007.
- [11] L. Bi, D. Xu, L. Zhang, Y. Lin, D. Wang, T. Xie, Metal Ni-loaded g-C₃N₄ for enhanced photocatalytic H₂ evolution activity: the change in surface band bending, *Phys. Chem. Chem. Phys.* 17 (44) (2015) 29895–29905.
- [12] L. Bi, D. Meng, Q. Bu, Y. Lin, D. Wang, T. Xie, Electron acceptor of Ni decorated porous carbon nitride applied in photocatalytic hydrogen production, *Phys. Chem. Chem. Phys.* 18 (46) (2016) 31534–31541.
- [13] N. Zhao, L. Kong, Y. Dong, G. Wang, X. Wu, P. Jiang, Insight into the crucial factors for photochemical deposition of cobalt cocatalysts on g-C₃N₄ photocatalysts, *ACS Appl. Mater. Inter.* 10 (11) (2018) 9522–9531.
- [14] J. Wen, J. Xie, Z. Yang, R. Shen, H. Li, X. Luo, et al., Fabricating the robust g-C₃N₄ nanosheets/carbons/NiS multiple heterojunctions for enhanced photocatalytic H₂ generation: an insight into the trifunctional roles of nanocarbons, *ACS Sustain. Chem. Eng.* 5 (3) (2017) 2224–2236.
- [15] J. Yan, H. Wu, H. Chen, R. Jiang, S.F. Liu, Fe (III) doped NiS₂ nanosheet: a highly efficient and low-cost hydrogen evolution catalyst, *J. Mater. Chem. A* 5 (21) (2017) 10173–10181.
- [16] J. Fu, C. Bie, B. Cheng, C. Jiang, J. Yu, Hollow CoS_x polyhedrons act as high-efficiency cocatalyst for enhancing the photocatalytic hydrogen generation of g-C₃N₄, *ACS Sustain. Chem. Eng.* 6 (2) (2018) 2767–2779.
- [17] P. Tan, Y. Liu, A. Zhu, W. Zeng, H. Cui, J. Pan, Rational design of Z-scheme system based on 3D hierarchical CdS supported 0D Co₉S₈ nanoparticles for superior photocatalytic H₂ generation, *ACS Sustain. Chem. Eng.* 6 (8) (2018) 10385–10394.
- [18] Y. Hou, A.B. Laursen, J. Zhang, G. Zhang, Y. Zhu, X. Wang, et al., Layered nanojunctions for hydrogen-evolution catalysis, *Angew. Chem. Int. Ed.* 125 (13) (2013) 3709–3713.
- [19] K. Chang, M. Li, T. Wang, S. Ouyang, P. Li, L. Liu, et al., Drastic layer-number-dependent activity enhancement in photocatalytic H₂ Evolution over nMoS₂/CdS ($n \geq 1$) under visible light, *Adv. Energy Mater.* 5 (10) (2015) 1402279.
- [20] H. He, J. Lin, W. Fu, X. Wang, H. Wang, Q. Zeng, et al., MoS₂/TiO₂ edge-on heterostructure for efficient photocatalytic hydrogen evolution, *Adv. Energy Mater.* 6 (14) (2016) 1600464.
- [21] Y. Shi, B. Zhang, Recent advances in transition metal phosphide nanomaterials: synthesis and applications in hydrogen evolution reaction, *Chem. Soc. Rev.* 45 (6) (2016) 1529–1541.
- [22] R. Shen, J. Xie, H. Zhang, A. Zhang, X. Chen, X. Li, Enhanced solar fuel H₂ generation over g-C₃N₄ nanosheet photocatalysts by the synergistic effect of noble metal-free Co₂P cocatalyst and the environmental phosphorylation strategy, *ACS Sustain. Chem. Eng.* 6 (1) (2017) 816–826.
- [23] W. Bi, L. Zhang, Z. Sun, X. Li, T. Jin, X. Wu, et al., Insight into electrocatalysts as cocatalysts in efficient photocatalytic hydrogen evolution, *ACS Catal.* 6 (7) (2016) 4253–4257.
- [24] R. Song, B. Luo, J. Geng, D. Song, D. Jing, Photothermocatalytic hydrogen evolution over Ni₂P/TiO₂ for full-spectrum solar energy conversion, *Ind. Eng. Chem. Res.* 57 (23) (2018) 7846–7854.
- [25] R. Song, W. Zhou, B. Luo, D. Jing, Highly efficient photocatalytic H₂ evolution using TiO₂ nanoparticles integrated with electrocatalytic metal phosphides as cocatalysts, *Appl. Surf. Sci.* 416 (2017) 957–964.
- [26] Z. Sun, H. Zheng, J. Li, P. Du, Extraordinarily efficient photocatalytic hydrogen evolution in water using semiconductor nanorods integrated with crystalline Ni₂P cocatalysts, *Energy Environ. Sci.* 8 (9) (2015) 2668–2676.
- [27] W.-J. Ong, L.-L. Tan, Y.-H. Ng, S.-T. Yong, S.-P. Chai, Graphitic carbon nitride (g-C₃N₄)-based photocatalysts for artificial photosynthesis and environmental remediation: are we a step closer to achieving sustainability? *Chem. Rev.* 116 (12) (2016) 7159–7329.
- [28] N. Meng, J. Ren, Y. Liu, Y. Huang, T. Petit, B. Zhang, Engineering oxygen-containing and amino groups into two-dimensional atomically-thin porous polymeric carbon nitrogen for enhanced photocatalytic hydrogen production, *Energy Environ. Sci.* 11 (3) (2018) 566–571.
- [29] B. Luo, R. Song, D. Jing, Significantly enhanced photocatalytic hydrogen generation over graphitic carbon nitride with carefully modified intralayer structures, *Chem. Eng. J.* 332 (2018) 499–507.
- [30] B. Luo, R. Song, J. Geng, D. Jing, Y. Zhang, Facile preparation with high yield of a 3D porous graphitic carbon nitride for dramatically enhanced photocatalytic H₂ evolution under visible light, *Appl. Catal. B* 238 (2018) 294–301.
- [31] D. Masih, Y. Ma, S. Rohani, Graphitic C₃N₄ based noble-metal-free photocatalyst systems: a review, *Appl. Catal. B* 206 (2017) 556–588.
- [32] H. Wang, X. Zhang, Y. Xie, Photoresponsive polymeric carbon nitride-based materials: design and application, *Mater. Today* (2018).
- [33] A. Indra, A. Acharjya, P.W. Menezes, C. Merschjann, D. Hollmann, M. Schwarze, et al., Boosting visible-light-driven photocatalytic hydrogen evolution with an integrated nickel phosphide–carbon nitride system, *Angew. Chem. Int. Ed.* 56 (6) (2017) 1653–1657.
- [34] D. Zeng, W.J. Ong, Y. Chen, S.Y. Tee, C.S. Chua, D.L. Peng, et al., Co₂P nanorods as an efficient cocatalyst decorated porous g-C₃N₄ nanosheets for photocatalytic hydrogen production under visible light irradiation, *Part. Part. Syst. Charact.* 35 (1) (2018) 1700251.
- [35] S.-S. Yi, J.-M. Yan, B.-R. Wulan, S.-J. Li, K.-H. Liu, Q. Jiang, Noble-metal-free cobalt phosphide modified carbon nitride: an efficient photocatalyst for hydrogen generation, *Appl. Catal. B* 200 (2017) 477–483.
- [36] L. Bi, X. Gao, L. Zhang, D. Wang, X. Zou, T. Xie, Enhanced photocatalytic hydrogen evolution of NiCoP/g-C₃N₄ with improved separation efficiency and charge transfer efficiency, *ChemSusChem* 11 (1) (2018) 276–284.
- [37] S. Cao, Y. Chen, H. Wang, J. Chen, X. Shi, H. Li, et al., Ultrasmall CoP nanoparticles as efficient cocatalysts for photocatalytic formic acid dehydrogenation, *Joule* 2 (3) (2018) 549–557.
- [38] X.-J. Sun, D.-D. Yang, H. Dong, X.-B. Meng, J.-L. Sheng, X. Zhang, et al., ZIF-derived CoP as a cocatalyst for enhanced photocatalytic H₂ production activity of g-C₃N₄, *Sustain. Energy Fuels* 2 (3) (2018) 1356–1361.
- [39] X.-J. Wang, X. Tian, Y.-j. Sun, J.-y. Zhu, F.-T. Li, H.-Y. Mu, et al., Enhanced Schottky effect of 2D–2D CoP/g-C₃N₄ interface for boosting photocatalytic H₂ evolution, *Nanoscale* 10 (26) (2018) 12315–12321.
- [40] D. Zeng, W. Xu, W.-J. Ong, J. Xu, H. Ren, Y. Chen, et al., Toward noble-metal-free visible-light-driven photocatalytic hydrogen evolution: monodisperse sub-15 nm Ni₂P nanoparticles anchored on porous g-C₃N₄ nanosheets to engineer 0D–2D heterojunction interfaces, *Appl. Catal. B* 221 (2018) 47–55.
- [41] N. Shi, W. Cheng, H. Zhou, T. Fan, M. Niederberger, Facile synthesis of mono-disperse Co₃O₄ quantum dots with efficient oxygen evolution activity, *Chem. Commun.* 51 (7) (2015) 1338–1340.
- [42] J. Xu, J. Wu, L. Luo, X. Chen, H. Qin, V. Dravid, et al., Co₃O₄ nanocubes homogeneously assembled on few-layer graphene for high energy density lithium-ion batteries, *J. Power Sources* 274 (2015) 816–822.
- [43] D. Potoczna-Petru, L. Kepiński, Reduction study of Co₃O₄ model catalyst by electron microscopy, *Catal. Lett.* 73 (1) (2001) 41–46.
- [44] D. Li, L.-X. Ding, S. Wang, D. Cai, H. Wang, Ultrathin and highly-ordered CoO nanosheet arrays for lithium-ion batteries with high cycle stability and rate capability, *J. Mater. Chem. A* 2 (16) (2014) 5625–5630.
- [45] F.D. Wu, Y. Wang, Self-assembled echinus-like nanostructures of mesoporous CoO nanorod@CNT for lithium-ion batteries, *J. Mater. Chem.* 21 (18) (2011) 6636–6641.
- [46] X. Yang, A.-Y. Lu, Y. Zhu, M.N. Hedhili, S. Min, K.-W. Huang, et al., CoP nanosheet assembly grown on carbon cloth: a highly efficient electrocatalyst for hydrogen generation, *Nano Energy* 15 (2015) 634–641.
- [47] H. Zhao, P. Jiang, W. Cai, Graphitic C₃N₄ decorated with CoP co-catalyst: enhanced and stable photocatalytic H₂ evolution activity from water under visible-light irradiation, *Chem. Asian J.* 12 (3) (2017) 361–365.
- [48] Y. Kang, Y. Yang, L.C. Yin, X. Kang, L. Wang, G. Liu, et al., Selective breaking of hydrogen bonds of layered carbon nitride for visible light photocatalysis, *Adv. Mater.* 28 (30) (2016) 6471–6477.
- [49] B. Luo, R. Song, J. Geng, D. Jing, Z. Huang, Strengthened spatial charge separation over Z-scheme heterojunction photocatalyst for efficient photocatalytic H₂ evolution, *Appl. Surf. Sci.* 475 (2019) 453–461.
- [50] Q. Han, Z. Cheng, B. Wang, H. Zhang, L. Qu, Significant enhancement of visible-light-driven hydrogen evolution by structure regulation of carbon nitrides, *ACS Nano* 12 (6) (2018) 5221–5227.
- [51] Y. Hong, C. Li, Z. Fang, B. Luo, W. Shi, Rational synthesis of ultrathin graphitic carbon nitride nanosheets for efficient photocatalytic hydrogen evolution, *Carbon* 121 (2017) 463–471.
- [52] X. She, L. Liu, H. Ji, Z. Mo, Y. Li, L. Huang, et al., Template-free synthesis of 2D porous ultrathin nonmetal-doped g-C₃N₄ nanosheets with highly efficient photocatalytic H₂ evolution from water under visible light, *Appl. Catal. B* 187 (2016) 144–153.
- [53] Y. Peng, L. Wang, Y. Liu, H. Chen, J. Lei, J. Zhang, Visible-light-driven photocatalytic H₂O₂ production on g-C₃N₄ loaded with CoP as a noble metal free co-catalyst, *Eur. J. Inorg. Chem.* 2017 (40) (2017) 4797–4802.
- [54] Y. Cao, S. Chen, Q. Luo, H. Yan, Y. Lin, W. Liu, et al., Atomic-level insight into optimizing the hydrogen evolution pathway over a Co₁-N₄ single-site photocatalyst, *Angew. Chem. Int. Ed.* 129 (40) (2017) 12359–12364.
- [55] W. Lei, Y. Mi, R. Feng, P. Liu, S. Hu, J. Yu, et al., Hybrid 0D–2D black phosphorus quantum dots–graphitic carbon nitride nanosheets for efficient hydrogen evolution, *Nano Energy* 50 (2018) 552–561.
- [56] L. Jing, R. Zhu, D.L. Phillips, J.C. Yu, Effective prevention of charge trapping in graphitic carbon nitride with nanosized red phosphorus modification for superior photo (electro) catalysis, *Adv. Funct. Mater.* 27 (46) (2017) 1703484.
- [57] Y. Dong, L. Kong, P. Jiang, G. Wang, N. Zhao, H. Zhang, et al., A general strategy to fabricate Ni_xP as highly efficient cocatalyst via photoreduction deposition for hydrogen evolution, *ACS Sustain. Chem. Eng.* 5 (8) (2017) 6845–6853.
- [58] S. Cao, Y. Chen, C.-C. Hou, X.-J. Lv, W.-F. Fu, Cobalt phosphide as a highly active non-precious metal cocatalyst for photocatalytic hydrogen production under visible light irradiation, *J. Mater. Chem. A* 3 (11) (2015) 6096–6101.
- [59] X. She, J. Wu, J. Zhong, H. Xu, Y. Yang, R. Vajtai, et al., Oxygenated monolayer carbon nitride for excellent photocatalytic hydrogen evolution and external quantum efficiency, *Nano Energy* 27 (2016) 138–146.
- [60] W. Shi, F. Guo, H. Wang, M. Han, H. Li, S. Yuan, et al., Carbon dots decorated the exposing high-reactive (111) facets CoO octahedrons with enhanced photocatalytic activity and stability for tetracycline degradation under visible light irradiation, *Appl. Catal. B* 219 (2017) 36–44.
- [61] P. Liu, J.A. Rodriguez, Catalysts for hydrogen evolution from the [NiFe] hydrogenase to the Ni₂P (001) surface: the importance of ensemble effect, *J. Am. Chem. Soc.* 127 (42) (2005) 14871–14878.
- [62] E. Skúlason, V. Tripkovic, M.E. Björkertun, Sd. Guðmundsdóttir, G. Karlberg, J. Rossmeisl, et al., Modeling the electrochemical hydrogen oxidation and evolution reactions on the basis of density functional theory calculations, *J. Phys. Chem. C* 114 (42) (2010) 18182–18197.
- [63] J. Li, M. Yan, X. Zhou, Z.-Q. Huang, Z. Xia, C.-R. Chang, et al., Mechanistic insights on ternary Ni_{2-x}Co_xP for hydrogen evolution and their hybrids with graphene as highly efficient and robust catalysts for overall water splitting, *Adv. Funct. Mater.*

- 26 (37) (2016) 6785–6796.
- [64] G. Zhang, A. Savateev, Y. Zhao, L. Li, M. Antonietti, Advancing the $n \rightarrow \pi^*$ electron transition of carbon nitride nanotubes for H₂ photosynthesis, *J. Mater. Chem. A* 5 (25) (2017) 12723–12728.
- [65] W. Jiang, X. Zong, L. An, S. Hua, X. Miao, S. Luan, et al., Consciously constructing heterojunction or direct Z-scheme photocatalysts by regulating electron flow direction, *ACS Catal.* 8 (3) (2018) 2209–2217.
- [66] M. Wang, L. Sun, J. Cai, P. Huang, Y. Su, C. Lin, A facile hydrothermal deposition of ZnFe₂O₄ nanoparticles on TiO₂ nanotube arrays for enhanced visible light photocatalytic activity, *J. Mater. Chem. A* 1 (39) (2013) 12082–12087.
- [67] X. Wang, K. Maeda, A. Thomas, K. Takanabe, G. Xin, J.M. Carlsson, et al., A metal-free polymeric photocatalyst for hydrogen production from water under visible light, *Nat. Mater.* 8 (1) (2009) 76.
- [68] B. Zhu, L. Zhang, B. Cheng, J. Yu, First-principle calculation study of tri-s-triazine-based g-C₃N₄: a review, *Appl. Catal. B* 224 (2018) 983–999.
- [69] J. Li, D. Wu, J. Iocozzia, H. Du, X. Liu, Y. Yuan, et al., Achieving efficient incorporation of Π -electrons into graphitic carbon nitride for markedly improved hydrogen generation, *Angew. Chem. Int. Ed.* (2018).
- [70] M. Rahman, K. Davey, Enabling Pt-free photocatalytic hydrogen evolution on polymeric melon: role of amorphization for overcoming the limiting factors, *Phys. Rev. Mater.* 2 (12) (2018) 125402.
- [71] W. Che, W. Cheng, T. Yao, F. Tang, W. Liu, H. Su, et al., Fast photoelectron transfer in (C_ring)-C₃N₄ plane heterostructural nanosheets for overall water splitting, *J. Am. Chem. Soc.* 139 (8) (2017) 3021–3026.
- [72] C. Li, Y. Du, D. Wang, S. Yin, W. Tu, Z. Chen, et al., Unique P-Co-N surface bonding states constructed on g-C₃N₄ nanosheets for drastically enhanced photocatalytic activity of H₂ evolution, *Adv. Funct. Mater.* 27 (4) (2017) 1604328.